processes

MDPI

Article

Study on the Preparation of Metallic Aluminum Powder by Nitrogen Atomization

Xiaoyun Yu, Jiasheng Yang, Guozhi Wang, Qingchun Yu *, Yong Deng * and Weijin Yu

National Engineering Research Center of Vacuum Metallurgy, Faculty of Metallurgical and Energy Engineering, Kunming University of Science and Technology, Kunming 650093, China; 15180133779@163.com (X.Y.); 13803402861@163.com (J.Y.); 17864889995@163.com (G.W.); 17853583621@163.com (W.Y.)
* Correspondence: yqcy@163.com (Q.Y.); dengxinnuo@126.com (Y.D.)

Abstract

Metal additive manufacturing represents the most promising application for Three-dimensional printing systems. Gas atomization is an important method for the preparation of metal powders. In this work, aluminum powders were prepared via vacuum induction atomization. Morphology and microstructure were investigated. Results demonstrated that optimal atomization occurred at 3 MPa with a 2.5 mm delivery tube diameter, yielding powders with an average particle size of 63.8 μm and a sphericity of more than 90%. Variations in droplet size caused differential cooling rates, enabling rapidly solidified small droplets to adhere to incompletely cooled large droplets and form satellite spheres. Quantitative analysis confirmed a positive correlation between metal powder particle size and surface satellite spheres. Large droplets exhibited long cooling times, resulting in more pronounced dendritic microstructures. This study provides theoretical insights for the preparation of metal powders.

Keywords: gas atomization; metal powder; satellite spheres; aluminium powder; particle size distribution

check for updates

Academic Editors: Edwan Anderson Ariza Echeverri and Crispulo Enrique Deluque Toro

Received: 30 June 2025
Revised: 18 September 2025
Accepted: 30 September 2025
Published: 13 October 2025

Citation: Yu, X.; Yang, J.; Wang, G.; Yu, Q.; Deng, Y.; Yu, W. Study on the Preparation of Metallic Aluminum Powder by Nitrogen Atomization. *Processes* **2025**, *13*, 3264. https://doi.org/10.3390/pr13103264

Copyright: © 2025 by the authors. Licensee MDPI, Basel, Switzerland. This article is an open access article distributed under the terms and conditions of the Creative Commons Attribution (CC BY) license (https://creativecommons.org/licenses/by/4.0/).

1. Introduction

Recent technological advancements have enabled the fabrication of geometrically complex metal components with high precision, offering unique advantages in customized production and flexible manufacturing [1], thereby significantly accelerating the development of the advanced manufacturing sector. Three-dimensional printing technology, known as additive manufacturing (AM) [2], has emerged as one of the most rapidly advancing innovations in the intelligent manufacturing era. Three-dimensional objects are constructed by sequentially depositing fine material powders based on digital models. Metal powder remains critical for component-specific printing, necessitating a comprehensive evaluation of part geometry, dimensional accuracy, mechanical strength, metal compatibility, cost efficiency, production speed, and batch size [3]. Typically, there are three powder manufacturing routes: chemical, physical, and mechanical [4]. Milling, electrolytic, and atomization methods are amongst the most popular production methods.

Atomization method offers high quality of produced aluminium alloy particles and prospects for mass production [5]. In this method [6], the metal to be atomised is first melted and then exposed to a high-velocity gas jet which causes the liquid metal to break up into small droplets. These droplets subsequently solidify in flight to form the aluminium alloy powder. Studies demonstrate that fine gas-atomized metal zirconium powders

exhibit small particle sizes, high sphericity, and part longevity [7]. N. Ciftci et al. [8] prepared iron-based glass powders using argon gas at different temperatures, revealing that hot gas atomization is helpful to produce particles with narrower size distributions and lower gas consumption. Hussain et al. [9] found that high-temperature gas atomization promotes more melt fragmentation into finer steel droplets than low-temperature processes. Li et al. [10] investigated the atomization of three kinds of Al alloys using melt nozzles with different inner diameters. They found that production of high-aluminium alloy powder with small average particle size occurred at the concave position of the delivery tube. The low production was at the flush position of the delivery tube with large average particle size. Microscopic morphology and solidification structure of fine powders significantly influence mechanical properties. Pinotti et. al. [11] evaluated the influence of melt feed nozzle diameter, superheating temperature, and atomization pressure on AA2017 aluminium alloy powder. Based on the venturi phenomenon, metal aluminium powder of different sizes and shapes can be produced [12]. Current gas atomization studies focus on the influence of powder preparation process on powder properties and yield, but few investigations on microstructural characteristics of powder have been reported.

In practical applications, the microstructure of particle will be designed according to the target performance. The particle shape will affect the fluidity, packing characteristics, and interface interaction of the particles. The internal crystal structure of powder including crystal form, phase composition, and defect affects the atomic diffusion ability inside the powders, which is the core determinant of the mechanical, electrical, magnetic, and other properties of powder materials. For example, spherical, fine-grained, and narrow-distribution powder should be used for the preparation of high-density parts; particle with rough, porous, and defect-rich microstructure suit highly active catalysts. So, understanding the relationship between microstructure and performance is important for achieving high performance of powder materials. In this work, aluminum powder was produced via vacuum induction gas atomization. Characterization and optimization between particle shape, particle size, surface morphology, crystal structure, and process parameters was made. Satellite particle, outgrowth index, and secondary dendritic arm spacing were also investigated.

2. Materials and Methods

Aluminium powder was prepared using gas atomization techniques. The schematic of equipment and atomization device was shown in Figure 1. During the experiment, the atomization pressure was selected as 1.0, 2.0, 3.0 and 4.0 MPa, and the inner diameters of the deflector tubes were 2.5, 3.0, 3.5 and 4.0 mm, respectively. and the angle of the atomizing nozzle, the degree of superheat of the melt, and the length of the guide tube were 30°, 200 °C, and 120 mm, with all processed under vacuum. Each group of experiments was repeated three time. The nitrogen atomization system consists of an atomization chamber, a power system, a vacuum system, and a nitrogen supplier system. The atomization chamber has an observation window with a diameter of 30 cm, with a temperature thermocouple, a pressure sensor, and a heating wire. Nitrogen was introduced into the atomization device through nozzle at a certain angle to atomize liquid aluminum during the experiment. Nitrogen pressure adjustment can be acquried by controlling the air valve. The kinetic energy carried by the high-speed gas flow is used to impact the molten aluminum entering the atomization zone, atomizing the molten metal into tiny droplets. These droplets are cooled and solidified into powders in an atomization furnace. The angle of the atomizing nozzle, the degree of superheat of the melt, and the length of the delivery tube were 30°, 200 °C, and 120 mm, respectively. Variable parameters of the atomization pressure and the inner diameters of the delivery tube were shown in Table 1. The optimal parameters were obtained according to particle size.

Table 1. Variable parameters.

Variables	Atomization Pressure (MPa)	Inner Diameter of Delivery Tube (mm)
Parameters	1.0 2.0 3.0 4.0	2.5 3.0 3.5 4.0

Powders are then classified by sieving into size ranges appropriate for various applications. Nitrogen was used to atomize the molten aluminum metal into powders.

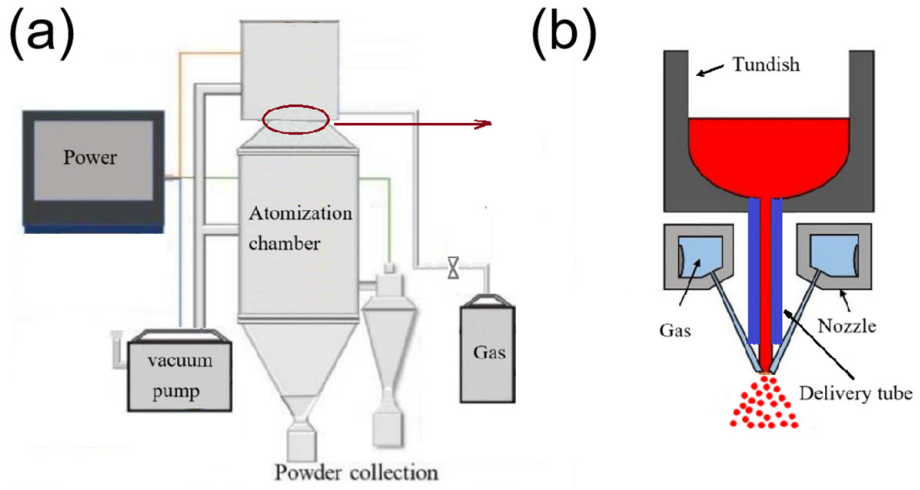

Figure 1. The structure and working principle of metal atomization equipment. (**a**) The structure of atomization equipment. (**b**) The principle of atomization equipment.

Particle Size Distribution (PSD) was analyzed using a MASTERSIZER 2000 laser (particle size analyzer. Powder morphology and surface elemental distribution were characterized using Field Emission Scanning Electron Microscopy (FESEM; Zeiss Sigma 300) coupled with Energy Dispersive Spectroscopy (EDS). Primary dendrite arm lengths within differently sized powders were quantified using Image J(imagej 1.53k) software. Nitrogen content was measured by HORIBA EMGA-830 oxygen-nitrogen-hydrogen analyzer.

3. Results

3.1. Effect of Atomization Pressure on Powder Particle Size

Figure 2a shows the cumulative distribution curve of particle size of aluminium metal powder at different pressures, and Figure 2b shows the relationship between atomization pressure and average particle size. Increasing pressure from 1 MPa to 3 MPa shifts the cumulative distribution curve leftward with an increase of 0–100 μm particles ratio from 52% to 68% and reduction of the average particle size from 132.7 μm to 63.8 μm. This demonstrates that higher atomization pressure promotes powder refinement of aluminum particles. However, with a further increase of pressure to 4 MPa, the cumulative distribution almost coincides with that of 3 MPa. Only a small increase occurred for particle size, from 63.8 μm to 72.6 μm. The fragmentation process of liquid aluminum droplets includes primary fragmentation, secondary fragmentation, and solidification [13]. The fragmentation of aluminum droplets relies on the kinetic energy provided by high-speed gas flow. As shown in Equation (1), the kinetic energy of the gas is affected by the gas velocity and flow rate.

$$E_k = \frac{1}{2}mv^2 \quad (1)$$

where m is the gas flow rate, v is the gas velocity, and E_k is the kinetic energy of the gas. According to Equation (1), the increase in flow rate leads to an increase in the kinetic energy of the gas, which makes the aluminum droplets break up more fully. When the influence of droplet temperature changes on the particle surface is ignored, the specific surface energy Q_w of the droplet is in a direct proportional relationship with the specific surface area [14]. The specific surface energy Q_w is as follows:

$$Q_w = L\frac{6}{\rho_m D_m} \quad (2)$$

where ρ_m is the density of the metal, D_m is the diameter of the droplet, L is a constant. As can be seen from Equation (2), surface energy of a metal droplet is inversely proportional to its diameter D_m. With the increase of atomization gas pressure from 1 MPa to 3 MPa, the impact of the gas on the liquid aluminium droplet becomes intense. Therefore, an appropriate increase in the atomising gas pressure can improve the surface energy of the droplets, and the powder can be refined.

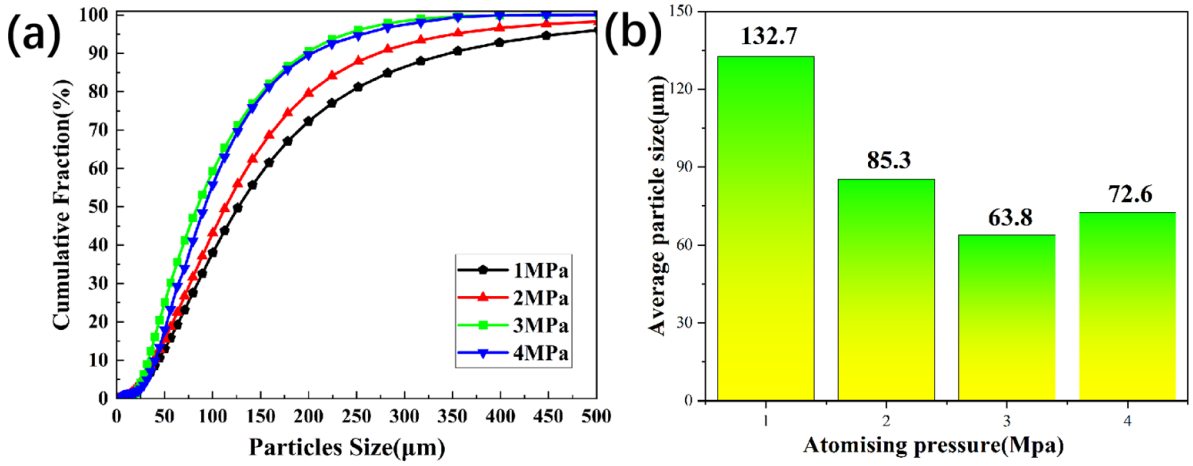

Figure 2. (**a**) Cumulative distribution curve of aluminium powder particle size; (**b**) Relationship between atomization pressure and average particle size.

Figure 3 presents SEM micrographs of spherical aluminum powders produced at different atomization pressures. Low gas pressure leads to the insufficient gas kinetic energy, which makes it difficult to break the liquid aluminum into spherical powders completely. The aluminum powders exhibits significant flaky and lumpy irregularities as shown in Figure 3a. As the gas pressure increases to 2 MPa, the powder particle size decreases significantly and shows regular spherical characteristics. It is worth noting that there are still some unbroken aluminium bands and ellipsoidal powders. At 3 MPa, the droplets undergo efficient primary and secondary fragmentation. Under conditions of large surface energy, a highly spherical degree of fine aluminum powder is produced as shown in Figure 3c. With the increase of atomization pressure, it is found that the proportion of fine powder is significantly reduced at 4 MPa, and the particle agglomeration occurs.

At 4 MPa the gas flow in the atomization zone below the nozzle fluctuates violently, and the aluminum droplets with high speed movement collide frequently in the restricted space, resulting in the rapid solidification of small-sized droplets attached to the surface of large droplets to produce a satellite sphere. As shown in Figure 3, the optimal atomization pressure is 3 MPa.

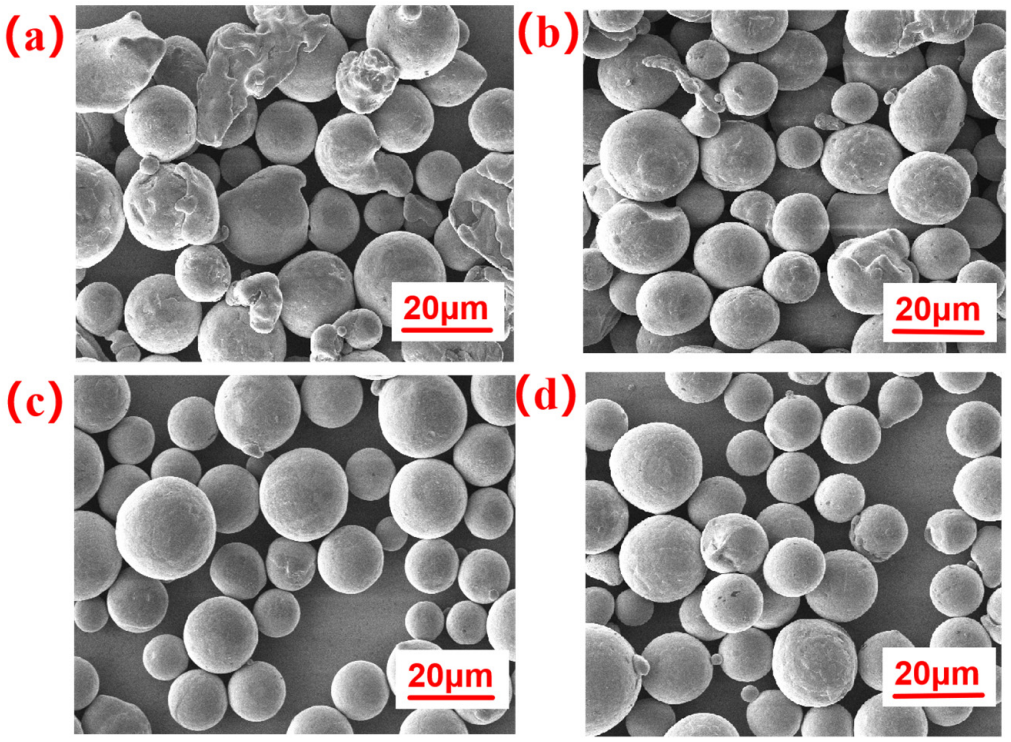

Figure 3. Aluminum powder morphology at different gas pressures. (**a**) The pressures is 1 MPa; (**b**) The pressures is 2 MPa; (**c**) The pressures is 3 MPa; (**d**) The pressures is 4 MPa.

3.2. Effect of Delivery Tube on the Powder Particle Size

The cumulative particle size distribution follows a lognormal pattern with curves shifting rightward as delivery tube diameter increases shown in Figure 4a. With the decrease in the diameter of delivery tube from 4.0 mm to 2.5 mm, the average particle size decreased from 80.2 μm to 57.4 μm. This demonstrates that the decrease of the delivery tube diameter promotes powder refinement. During gas atomization, capillary resistance plays an important role on the aluminum melt flow in the delivery tube. Capillary resistance is expressed by the Young Laplace equation [15]:

$$P_s = \frac{4\sigma\cos\theta}{D_0} \tag{3}$$

where D_0 is the guide tube's inner diameter, σ is the melt's surface tension, and θ is the liquid solid contact angle. Equation (3) indicates that capillary resistance is inversely proportional to D_0. A large D_0 will significantly reduce the capillary resistance. In other words, the amount of liquid aluminum flowing out from the delivery pipe increases, meaning the decrease of the surface energy of liquid aluminum. The diameter of the delivery tube negatively correlates with atomization efficiency. However, the liquid aluminum is easily solidified at the bottom of the guide tube due to the large capillary resistance, and the clogging phenomenon occurs leading to the failure of atomization. Meanwhile, the cumulative particle size distribution curve at a diameter of 2.5 mm is close to that of 3.0 mm. Considering these two aspects, the optimal powder performance is achieved at a diameter of 3.0 mm.

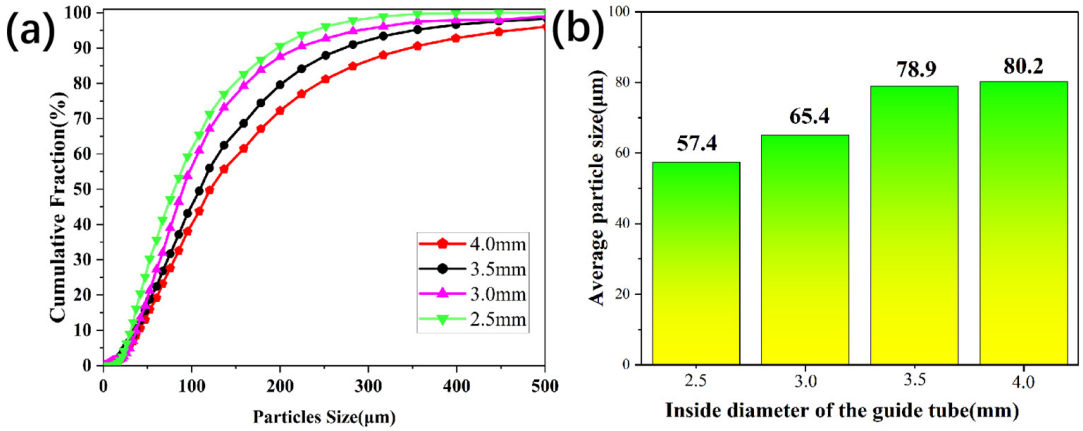

Figure 4. Diameter of delivery tube versus aluminum particle size: (**a**) Cumulative distribution; (**b**) average particle size.

3.3. Morphology and Element Distribution

Figure 5 depicts the surface morphology of aluminum powders at different scales, revealing irregular surfaces characterized by dendritic structures in the area pointed to by the purple arrow. Connections between dendrites form rose-shaped, cross-shaped, and various other irregular structures, which are retained on the powder surface. Satellite particles adhere to powder surfaces as the yellow arrows shown in Figure 5a,b. Figure 6 demonstrates nitrogen distribution on the aluminum powder surface. Nitrogen content remains consistent (0.36–0.43%) with low variability and uniform surface distribution. The results show that part of the nitrogen is dissolved when aluminium is molten.

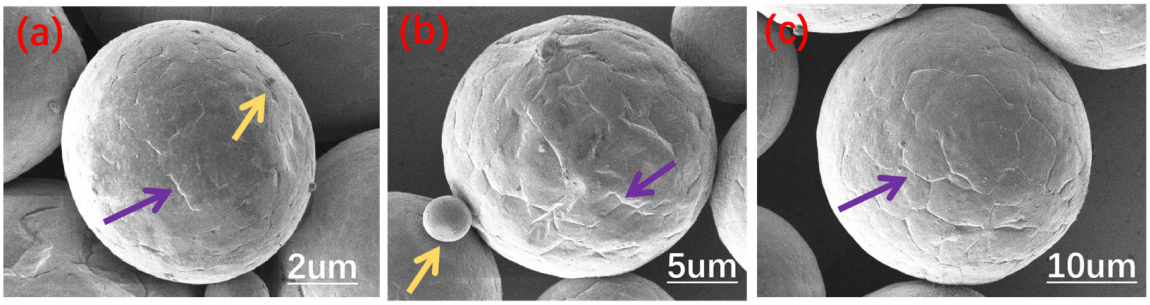

Figure 5. Surface morphology of powders with different particle sizes. (**a**) 2 μm; (**b**) 5 μm; (**c**) 10 μm.

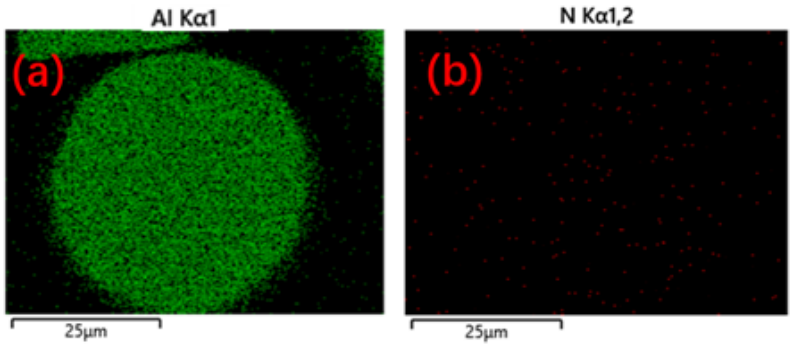

Figure 6. EDS analysis of aluminum powder. (**a**) Distribution of aluminum; (**b**) Distribution of N.

Figure 7 illustrates the internal morphology of the powder with different particle sizes. Fine cytosolic tissue structures between the dendrites are found along with hollow powders. As shown in Table 2, the distribution of nitrogen elements inside the powder is almost zero, which indicates that nitrogen exists only on the surface of powder.

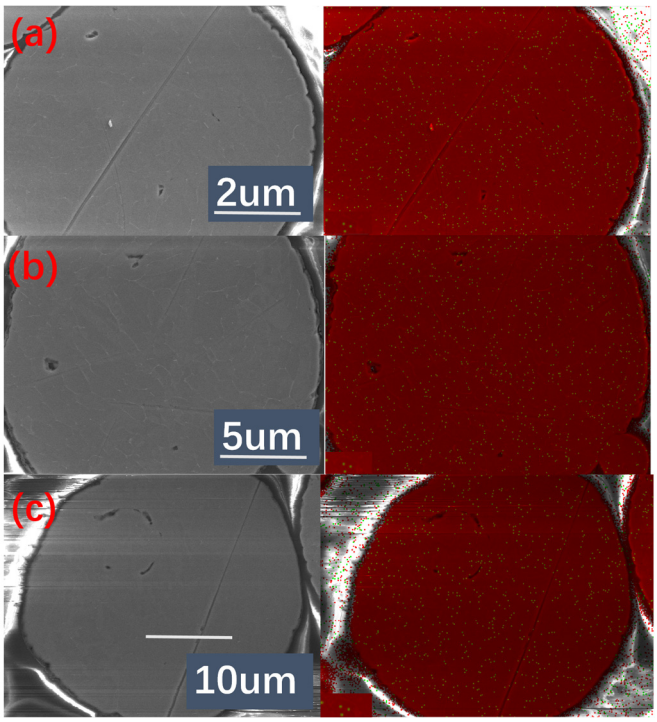

Figure 7. Internal morphology of aluminum powders with different sizes (**a**) 2 μm; (**b**) 5 μm; (**c**) 10 μm.

Table 2. Aluminum powder internal element content.

Aluminum Powder Size	Al Content (%)	Nitrogen Content (%)
2 μm	99.9	0
5 μm	99.7	0.1
10 μm	99.6	0.15

4. Discussion

4.1. Characterization of Outgrowth Index and Sphericity

Outgrowth index, defined as the ratio of the adhered satellite particles to the total surface features of particle, has been proposed to quantitatively assess satellite particles through digital filtering [16]. The outgrowth index 0, 50%, 66%, 75%, and 80% illustrates that there are 0, 1, 2, 3, and 4 satellite sphere on the surface, respectively. Standard deviation, which characterize the inhomogeneity of the powder, were incorporated for comparison [17]. Higher values are associated with large deviations in the motion states and solidification time of droplets, thus increasing the probability of collisions and the formation of satellite spheres. Fine particles have larger surface areas and high dispersion values, which are correlated with increasing surface energy per unit mass. The outgrowth index, standard deviation, and dispersion are described by Equations (4)–(6) [16,17]:

$$\eta = \left(1 - \frac{1}{n_{outgrowth}+1}\right) \times \% \quad (4)$$

$$\delta = \sqrt{\frac{\sum_{i=1}^{n} (d_i - \overline{d})^2}{n}} \quad (5)$$

$$\text{span} = \frac{D_{90} - D_{10}}{D_{50}} \quad (6)$$

where $n_{outgrowth}$ is the number of adherent particles, δ is the standard deviation, d_i is the particle size of any particle, d_i is represents the particle size of any particle, and $\overline{d}$ is the average particle size. Based on the analysis in Figure 8, aluminum powder exhibits relatively high density; and the number of satellite spheres has more ratio among powders with larger particle size and more irregular shape, which reduces the powder density of aluminum powder.

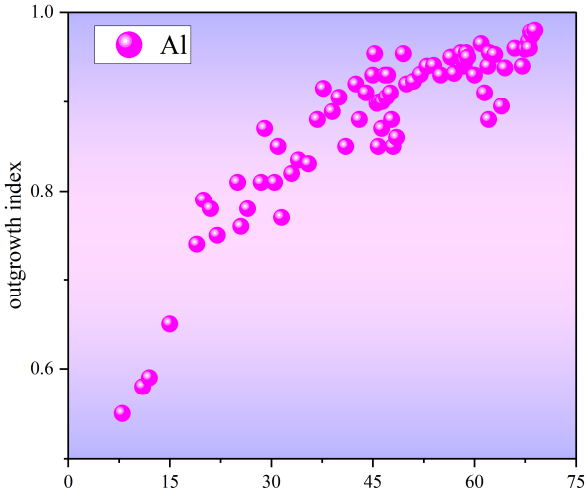

Figure 8. Relationship between outgrowth index and powder particle size.

Aluminum particles prepared at the pressure of 3 MPa were used to make an assessment of the surface characteristics. Based on Equations (4)–(6), Outgrowth, standard deviation and span were obtained in Table 3.

Table 3. Experimental parameters at atmospheric pressure of 3 MPa.

Parameters	Al
Outgrowth = 0	76%
Standard deviation	54.6
span	1.91

Sphericity offers a rigorous way to describe the shape of the powder particles. The calculation formula for the sphericity is as follows [18]:

$$W_V = \frac{1}{\sqrt{\overline{V}-1}}, \ \overline{V} = \frac{1}{N}\sum_{i=1}^{i=N}\left(1+\frac{\lambda_E}{\lambda_i}\right)^2 \quad (7)$$

where V is the particle volume, λ_E is the diameter of the largest internally connected sphere, and λ_i is the diameter of the internally connected disc at the i point where the sphere contains the particle profile.

Powder flowability is a very critical concept in powder metallurgy, additive manufacturing (3D printing), metal injection molding, and other industries. Metal powder fluidity refers to the difficulty and speed of metal powder flow under specific conditions. Simply put, it measures the ability of powder to "flow" like liquid. Liquid powders can quickly, uniformly, and steadily fill the mold or spread on the printing platform, while poorly liquid powders are likeas to agglomery and bridge, resulting in uneven filling and ultimately affecting product quality.

The most accurate quantification of sphericity is bluntness. the bluntness of the powders at different powder sizes are shown in Figure 9. It can be seen that in the powders with particle size of 0–60 μm, the larger the powder size is, the tends to increase. The

bluntness of the majority of powders exceeds 90%. This means that most of the aluminum powders exhibit a high sphericity.

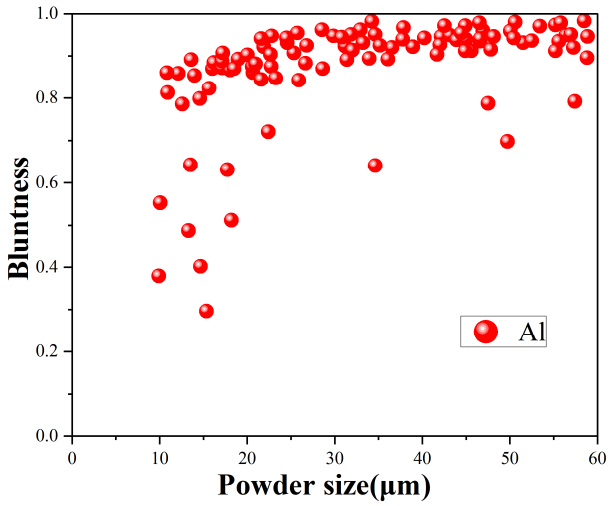

Figure 9. Relationship between powder particle size and obtuseness.

4.2. The Process of Dendrite Generation

Figure 10 depicts the surface and internal dendritic structures of aluminum powders, respectively. According to the dendrite growth model (Figure 11) [19], small powder particles experience distinct pressure difference between their surfaces and interiors, creating different cooling rates. Surface regions develop cellular structures with primary dendrites, following by the honeycomb microstructures surrounding nucleation sites internally. With the increase of droplet size, the cooling rate decreases, and the overall solidification time increases, providing kinetic conditions for the growth of secondary dendritic structures. Eventually, the growth of primary dendritic arms on the surface and inside of the solidified particles is strengthened, and the spacing of secondary dendritic arms increases. As droplet size continues to increase, the solidification rate decreases significantly, and secondary dendrites form and grow freely inside the powder. Surface energy leads to a fast diffusion of liquid aluminum at the edges of the microstructure. Inside of the droplet with relatively low temperature change (ΔT) produces a disordered small-sized equiaxed microstructure during cooling process. Meanwhile, the morphology of the equiaxed microstructures tends to be a spherical state due to the increase of particle size, and the liquid aluminum diffusion makes the equiaxed microstructures more uniform.

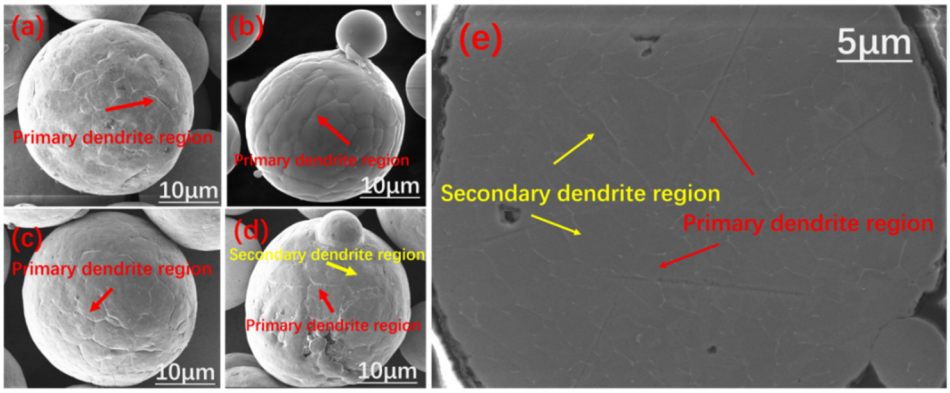

Figure 10. Structures of aluminum powder: (**a**–**d**) Surface dendrites; (**e**) Internal dendrites.

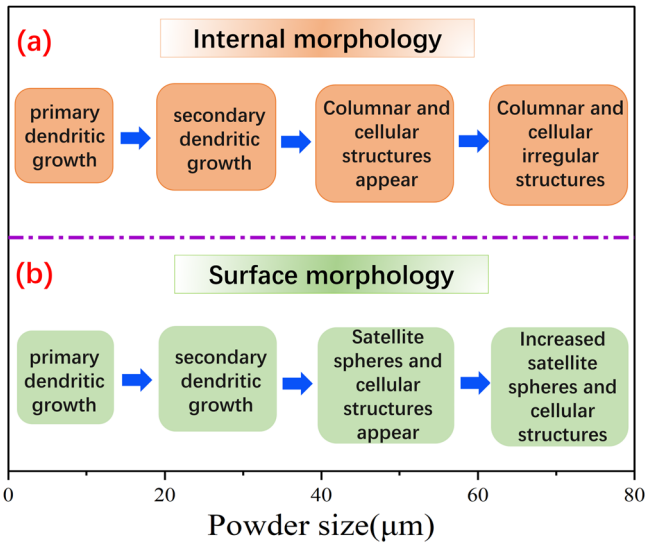

Figure 11. Dendrite growth model: (**a**) Internal morphology. (**b**) Surface morphology.

The nucleation sites of primary dendrites are located at sub-boundary positions. The length of primary dendrite arms is no more than the particle size, which can be approximately regarded as the size of the solidified powder. Figure 12 shows the variation curves of primary dendrite arm spacing with different powder sizes. When the particle size increases from 0 to 45 μm, the length of primary dendrite arms also increases from 0 to ~30 μm. As the particle size continues to grow, the length of primary dendrite arms remains stable around 30 μm. For the pure aluminum particles, influence of the trace elements in aluminum on the atomization can be ignored. No dendrite structures should be produced under conditions of the same diffusion coefficient. This abnormal phenomenon is probably related to thermal properties such as solidification enthalpy and specific heat capacity, indicating that the evolution of the microstructure is influenced by multiple factors.

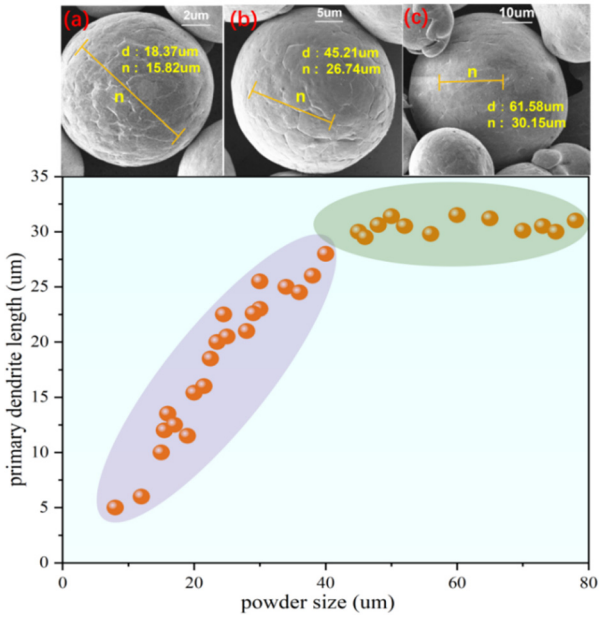

Figure 12. Aluminium powder particle size d versus primary dendrite λ spacing. (**a**) 2 μm; (**b**) 5 μm; (**c**) 10 μm.

The secondary Dendrite Arm Spacing (SDAS) is an essential parameter for the assessment of the particle refinement. The SDAS values, obtained by Image J analysis, are listed in Table 4. Relationship between the SDAS and the particle size is graphically presented in

Figure 13. There is a clear linear dependence of SDAS on the powder dimensions, exhibiting progressive expansion from 0.5 μm to 2.5 μm. The fitting relationship is determined by [20]:

$$\lambda = 0.5 + 0.021\mathrm{d} \left(\mathrm{R}^2 = 0.96\right) \tag{8}$$

Additionally, a solidification rate using a calibration equation for the spacing of the secondary dendrite arms and the solidification rate is [21]:

$$\lambda = \beta \left(\frac{\mathrm{dT}}{\mathrm{dt}}\right)^{-\frac{1}{3}} \tag{9}$$

where β is a constant related to the material class. It can be found from Equation (9) that the cooling rate is negatively correlated with the particle size. The heat transfer coefficient of powders with large particle sizes is less than that of powders with small particle sizes, leading to a significant particle refinement.

Table 4. Variation curve of the secondary dendrite arm spacing as a function of the powder size.

d (μm)	30	40	52	64	78	86	95	112
λ (μm)	1.11	1.35	1.90	1.83	2.13	2.30	2.51	2.85

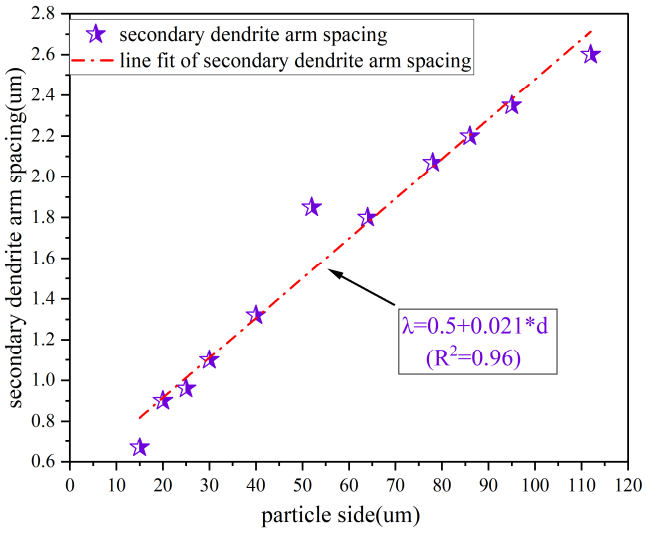

Figure 13. Aluminium powder particle size d versus secondary dendrite λ spacing.

Solidification of the atomized molten droplets goes through the nucleation, the growth of the primary dendrite and the secondary dendrite [22]. When the nucleation is completed, the growth of primary dendrites begins. The latent heat released by the droplets will generate a temperature change (ΔT) perpendicular to the primary dendrites, which is a necessary prerequisite for the formation of the secondary dendrites. It can be seen from Equation (9) that the spacing and growth of secondary dendrites are determined by the solidification rate. High solidification rate makes droplet with small particle sizes semi-solid, thereby inhibiting the growth of secondary dendrites. As a result, the secondary dendrites are mostly present in powders with larger particle sizes. Combining Formulas (8) and (9), the relationship between the particle size of the powder and the solidification time can be obtained [22].

$$\frac{dT}{dt} = \left(\frac{1809.1}{18.25 + d}\right)^3 \tag{10}$$

It can be seen from the Equation (10) that the existence of the temperature change rate provides a good kinetic foundation for the growth of dendritic structures. With the increase in the particle size, the temperature change rate decreases. The solidification time governs internal dendritic structure development. For fine powders with a size range of 0–35 μm, the rapid solidification of their surfaces gives rise to the cellular or dendritic surface structures during the atomization process. However, inside the fine powder, only primary dendrites can be observed. For large powders with a size more than 35 μm, the decrease of temperature change rate makes the overall solidification time increase. Secondary dendrites have sufficient kinetic conditions for growth, so primary dendrites and secondary dendrites coexist on the surface of the powder. In addition, since the cooling rate of satellite spherical powder is higher than that of the ordinary particles, the cooling rate at the interface is accelerated, leading to the formation of cellular structures at the interface of satellite powder.

4.3. The Process of Increasing Nitrogen on the Surface of the Powder

Figure 14 illustrates the variation in nitrogen content with particle size under different atomization pressures. For 10 μm powder, nitrogen content does not changes little at ~0.33 wt%. For the powders with a particle size of 150 μm, the nitrogen content increases to 0.23%, 0.30%, 0.43%, and 0.46% respectively, with the increase of atomization pressure. The powder surface can adsorb more free nitrogen during the atomization process when there is a large surface area on the particle. When the atomization pressure is low, finer powders have higher solidification rates, thus inhibiting the precipitation behavior of nitrogen. The nitrogen content decreases with the increase of powder particle size before 2.2 MPa. When the atomization pressure is more than 2.2 MPa and continually increases, the nitrogen content increases with the increase of powder particle size. Meanwhile, the enhancement of the kinetic energy of nitrogen gas may strengthen the energy exchange between the nitrogen gas and the liquid metal droplets. So, there is an increase in the nitrogen content. It can be inferred that the influence of specific surface area on nitrogen adsorption is less than that of solidification rate on the powder.

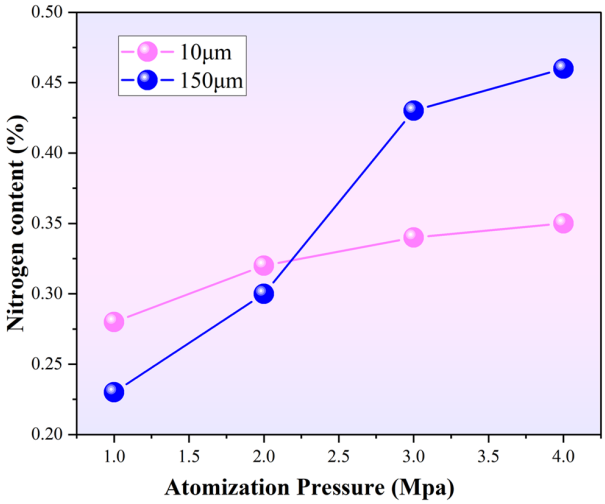

Figure 14. Effect of atomization pressure on nitrogen content of powder.

The nitrogen enhancement effect originates from nitrogen dissociation into atomic nitrogen during efficient atomization, accompanied by kinetic and surface energy conversion [23]. The dissociation and solidification behavior of nitrogen is a complex process. The nitrogen content of particles can be changed by controlling the particle size and atomization pressure. According to Dombrowski's wave fragmentation model [24], the key step of the

increase of nitrogen content is the melting process, not the atomization process. The main role is to accelerate the solidification of atomized droplets, thereby inhibiting the precipitation of nitrogen. In addition, high chamber pressure in the atomization furnace chamber can offer high melting pressure and solidification pressure to improve the solubility and inhibit precipitation of nitrogen, respectively. Thus, benefiting from the synergetic effect between atomization pressure and chamber pressure, the high nitrogen content powder can be finally obtained.

4.4. Formation of Satellite Powders

Satellite sphere particles are formed due to the differences in the solid-liquid morphology of the droplets and the formation of rapid collisions [25]. As shown in Figure 15, satellite sphere particles include three types: the first one is the point contact type shown in Figure 15a. The point contact satellite sphere is generated at the bottom of the atomization zone. When the metal droplet is about to solidify, it rapidly collides with other powders that are about to solidify or have already solidified. The second one is the surface contact type shown in Figure 15b; a surface contact type satellite sphere is generated in the middle of the atomized zone. During the solidification stage of the metal droplet, it undergoes rapid collisions with other powders that are about to solidify or have already solidified. The third one is the parcel type shown in Figure 15c. The encapsulated satellite spheres are generated in the upper part of the atomization zone. When the metal droplet is in the liquid stage, it undergoes rapid collisions with the solidified powders.

A recirculation zone, in which the particles are cooled at a slow rate, is formed due to the collision of nitrogen gas in the direction of the gas atomization nozzle. Most particles have temperatures more than the solidification point. Many particles have the opportunity to collide and produce satellite spheres. The solidification rate of particle near the nozzle outlet is relatively fast due to the low temperature in the vicinity of the nozzle outlet. Droplets with different sizes have different physical sensible heat. After cooling in the recirculation zone, there are three types of droplets with different temperatures [25]: high-temperature droplets, higher temperature droplets, and cryonic droplets. When cryonic droplets collides each other, they will produce point contact powders. As a cryonic droplet runs into a higher temperature droplet, a surface contact powder will be formed. Similarly, a parcel contact powder will grow up on the condition of collision between high temperature droplet and cryonic droplet. As shown in Figure 9, the number of satellite spheres significantly increases with the increase of powder particle size. It can be inferred that satellite spheres on the powder surface can be reduced by controlling of atomization parameters to achieve a specific powder particle size range.

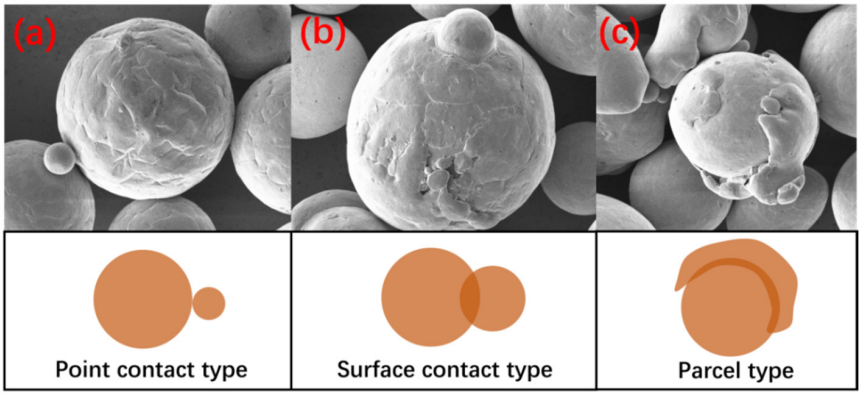

Figure 15. Several typical satellite powders cases. (**a**) Point contact type; (**b**) Surface contact type; (**c**) Parcel contact type.

5. Conclusions

Aluminum powders was prepared by means of vacuum induction atomization. Effects of atomization pressure and guide tube diameter on powder particle size were investigated. Morphology and microstructure are analyzed. Some meaningful results are obtained as follows:

(1) With the increase of atomization pressure, the proportion of 0–100 μm powder gradually increased from 52% to 68%, and the average particle size of the powder decreased from 132.7 μm to 63.8 μm. Conversely, increasing the guide tube inner diameter elevated average particle size from 57.4 μm to 80.2 μm.
(2) Although atomization process optimization significantly improved particle size distribution, there are defects such as satellite powder.
(3) Surface microstructure is mainly dendritic and cellular due to the adhesion of satellite spheres. The internal microstructure was affected by ΔT and dendrite remelting, and the microstructure evolved from dendrites to columnar isometric and spherical or sub-spherical isometric microstructure with increasing powder particle size.
(4) The nitrogen content in the powder increases with increasing pressure in the atomization chamber. High gas pressure can effectively inhibit the nitrogen precipitation behavior.

Author Contributions: Conceptualization, X.Y. and Q.Y.; methodology, Y.D.; software, X.Y.; validation, X.Y. and Y.D.; formal analysis, Q.Y., J.Y. and G.W.; investigation, X.Y. and W.Y.; resources, X.Y.; data curation, X.Y.; writing—original draft preparation, X.Y.; writing—review and editing, Q.Y.; visualization, X.Y.; supervision, Q.Y.; project administration, Q.Y.; funding acquisition, Q.Y. All authors have read and agreed to the published version of the manuscript.

Funding: This work was supported by the National Natural Science Foundation of China, grant number 52364054.

Data Availability Statement: The original contributions presented in this study are included in the article. Further inquiries can be directed to the corresponding authors.

Conflicts of Interest: The authors declare no conflicts of interest.

References

1. Ligon, S.C.; Liska, R.; Stampfl, J.; Gur, M.; Mülhaupt, R. Polymers for 3D Printing and Customized Additive Manufacturing. *Chem. Rev.* **2017**, *117*, 10212–10290. [CrossRef]
2. Kim, H.; Lee, S. Printability and physical properties of iron slag powder composites using material extrusion-based 3D printing. *J. Iron Steel Res. Int.* **2020**, *28*, 111–121. [CrossRef]
3. Khoo, Z.X.; Teoh, J.E.M.; Liu, Y.; Chua, C.K.; Yang, S.; An, J.; Leong, K.F.; Yeong, W.Y. 3D printing of smart materials-A review on recent progresses in 4D printing. *Virtual Phys. Prototyp.* **2015**, *10*, 103–122. [CrossRef]
4. Tsirlis, M.; Michailidis, N. Optimization of aluminium powder production through a novel ultralow pressure gas-atomization method. *CIRP Ann.* **2022**, *71*, 141–144. [CrossRef]
5. Bai, H.; Ji, Y.; Li, Y.; Wang, H.; Kang, X.; Ren, H.; Lv, W. Comparative Study on Preparation of Aluminum-Rare Earth Master Alloy Fine Powders by Mechanical Pulverization and Gas Atomization Methods. *Processes* **2025**, *13*, 548. [CrossRef]
6. Unal, A. Production of Rapidly Solidified Aluminium Alloy Powders by Gas Atomisation and Their Applications. *Powder Metall.* **1990**, *33*, 53–64. [CrossRef]
7. Zai, X.; Chen, S.; Wu, H.; Liu, Y. Preparation of Spherical High-Purity Zr Powders by Gas Atomization without Crucible. *Chin. J. Rare Met.* **2018**, *8*, 864–868. [CrossRef]
8. Ciftci, N.; Ellendt, N.; Barreto, E.S.; Mädler, L.; Uhlenwinkel, V. Increasing the amorphous yield of $\{(Fe_{0.6}Co0.4)_{0.75}B_{0.2}Si_{0.05}\}_{96}Nb_4$ powders by hot gas atomization. *Adv. Powder Technol.* **2018**, *29*, 380–385. [CrossRef]
9. Hussain, S.; Cui, C.; He, L.; Mädler, L.; Uhlenwinkel, V. Effect of hot gas atomization on spray forming of steel tubes using a close-coupled atomizer (CCA). *J. Mater. Process. Technol.* **2020**, *282*, 116677. [CrossRef]
10. Li, X.-G.; Zhu, Q.; Shu, S.; Fan, J.-Z.; Zhang, S.-M. Fine spherical powder production during gas atomization of pressurized melts through melt nozzles with a small inner diameter. *Powder Technol.* **2019**, *356*, 759–768. [CrossRef]

11. Pinotti, V.E.; Andreoli, A.F.; Gargarella, P. Gas atomization of AA2017 aluminum alloy: Effect of process parameters in the physical properties of powders for additive manufacturing. *J. Mater. Res. Technol.* **2024**, *30*, 3650–3662. [CrossRef]
12. Tsirlis, M.; Michailidis, N. Low-pressure gas atomization of aluminum through a Venturi nozzle. *Adv. Powder Technol.* **2020**, *31*, 1720–1727. [CrossRef]
13. Wei, M.; Chen, S.; Liang, J.; Liu, C. Effect of atomization pressure on the breakup of TA15 titanium alloy powder prepared by EIGA method for laser 3D printing. *Vacuum* **2017**, *143*, 185–194. [CrossRef]
14. Girin, A.G. Equations of the kinetics of droplet fragmentation in a high-speed gas flow. *J. Eng. Phys. Thermophys.* **2011**, *84*, 262–269. [CrossRef]
15. Elger, D.F.; Crowe, B.C.; Roberson, J.A.; Williams, B.C. *Engineering Fluid Mechanics, SI Version*; John Wiley & Sons: Hoboken, NJ, USA, 2015. [CrossRef]
16. Gao, C.F.; Xiao, Z.Y.; Zou, H.P.; Liu, Z.Q.; Chen, J.; Li, S.K.; Zhang, D.T. Characterization of spherical AlSi10Mg powder produced by double-nozzle gas atomization using different parameters. *Trans. Nonferrous Met. Soc. China* **2019**, *29*, 374–384. [CrossRef]
17. Sun, L.; Chow, L.C.; Bonevich, J.E.; Wang, T.; Mitchell, J.W. A new approach to prepare well-dispersed CaF(2) nanoparticles by spray drying technique. *J. Biomed. Mater. Res. Part B Appl. Biomater.* **2011**, *98B*, 223–229. [CrossRef]
18. Pirard, E.; Califice, A.; Léonard, A.; Gregoire, M. Multiscale Shape Analysis of Particles in 3D Using the Calypter. 2022. Available online: http://hdl.handle.net/2268/22089 (accessed on 11 September 2022).
19. Zhang, H.; Xu, Q.; Shi, Z.; Liu, B. Numerical simulation of dendrite grain growth of DD6 superalloy during directional solidification process. *Acta Metall. Sin.* **2014**, *50*, 345–354. [CrossRef]
20. Yamanoglu, R.; Zeren, M.; German, R.M. Solidification characteristics of atomized AlCu4Mg1-SiC composite powders. *J. Min. Metall.* **2012**, *48*, 73–79. [CrossRef]
21. Joly, P.A.; Mehrabian, R. Complex alloy powders produced by different atomization techniques: Relationship between heat flow and structure. *J. Mater. Sci.* **1974**, *9*, 1446–1455. [CrossRef]
22. Perepezko, J.; Sebright, J.; Höckel, P.; Wilde, G. Undercooling and solidification of atomized liquid droplets. *Mater. Sci. Eng. A* **2002**, *326*, 144–153. [CrossRef]
23. Weddeling, A.; Lefor, K.; Hryha, E.; Huth, S.; Nyborg, L.; Weber, S.; Theisen, W. Nitrogen uptake of nickel free austenitic stainless steel powder during heat treatment—An XPS study. *Surf. Interface Anal.* **2015**, *47*, 413–422. [CrossRef]
24. Dombrowski, N.; Johns, W.R. The aerodynamic instability and disintegration of viscous liquid sheets. *Chem. Eng. Sci.* **1963**, *18*, 203–214. [CrossRef]
25. Liu, C.; Li, X.; Shu, S.; Huang, Y.H.; Li, X.; Zhu, Q. Numerical investigation on flow process of liquid metals in melt delivery nozzle during gas atomization process for fine metal powder production. *Trans. Nonferrous Met. Soc. China* **2021**, *31*, 3192–3204. [CrossRef]

Disclaimer/Publisher's Note: The statements, opinions and data contained in all publications are solely those of the individual author(s) and contributor(s) and not of MDPI and/or the editor(s). MDPI and/or the editor(s) disclaim responsibility for any injury to people or property resulting from any ideas, methods, instructions or products referred to in the content.